

## Article

# Fe-Si Intermetallics/ $\text{Al}_2\text{O}_3$ Composites Formed between Fe-20% Si and Fe-70.5% Si by SHS Metallurgy Method

Chun-Liang Yeh , Ann Lu and Wei-Che Liang

Department of Aerospace and Systems Engineering, Feng Chia University, Taichung 40724, Taiwan

\* Correspondence: clyeh@fcu.edu.tw; Tel.: +886-4-2451-7250 (ext. 3963)

**Abstract:** Fe–Si intermetallics– $\text{Al}_2\text{O}_3$  composites were fabricated by thermite-assisted combustion synthesis. Combustion reactions were conducted with powder compacts composed of  $\text{Fe}_2\text{O}_3$ , Al, Fe, and Si. The starting stoichiometry of powder mixtures had an atomic Fe/Si proportion ranging from Fe-20% to Fe-70.5% Si to explore the variation of silicide phases formed with Si percentage. Combustion in the mode of self-propagating high-temperature synthesis (SHS) was achieved and the activation energy of the SHS reaction was deduced. It was found that the increase of Si content decreased the combustion temperature and combustion wave velocity. Three silicide compounds,  $\text{Fe}_3\text{Si}$ , FeSi, and  $\alpha\text{-FeSi}_2$ , along with  $\text{Al}_2\text{O}_3$  were identified by XRD in the final products.  $\text{Fe}_3\text{Si}$  was formed as the single-phase silicide from the reactions with Si percentage from Fe-20% to Fe-30% Si. FeSi dominated the silicide compounds in the reactions with atomic Si content between Fe-45% and Fe-55% Si. As the Si percentage increased to Fe-66.7% Si and Fe-70.5% Si,  $\alpha\text{-FeSi}_2$  became the major phase. The microstructure of the composite product showed that dispersed granular or nearly spherical iron silicides were embedded in  $\text{Al}_2\text{O}_3$ , which was dense and continuous. Most of the silicide grains were around 3–5  $\mu\text{m}$  and the atomic ratio of silicide particles from the EDS analysis confirmed the presence of  $\text{Fe}_3\text{Si}$ , FeSi, and  $\text{FeSi}_2$ .

**Keywords:** iron silicides– $\text{Al}_2\text{O}_3$  composites; SHS; Fe/Si proportion;  $\text{Fe}_3\text{Si}$ ; FeSi;  $\text{FeSi}_2$



**Citation:** Yeh, C.-L.; Lu, A.; Liang, W.-C. Fe-Si Intermetallics/ $\text{Al}_2\text{O}_3$  Composites Formed between Fe-20% Si and Fe-70.5% Si by SHS Metallurgy Method. *Metals* **2022**, *12*, 1337. <https://doi.org/10.3390/met12081337>

Academic Editors: Haiming Ding, Peng Wang and Xiangguang Kong

Received: 20 July 2022

Accepted: 9 August 2022

Published: 11 August 2022

**Publisher's Note:** MDPI stays neutral with regard to jurisdictional claims in published maps and institutional affiliations.



**Copyright:** © 2022 by the authors. Licensee MDPI, Basel, Switzerland. This article is an open access article distributed under the terms and conditions of the Creative Commons Attribution (CC BY) license (<https://creativecommons.org/licenses/by/4.0/>).

## 1. Introduction

Transition metal silicides have been considered as the potential structural materials for high-temperature applications due to their excellent high-temperature mechanical properties, good oxidation resistance, creep resistance, and thermal stability [1–3]. Particular attention has been paid to Fe–Si intermetallic compounds, as they possess magnetic, electronic, optical, mechanical, and catalytic properties on account of different crystal structures and phase compositions [4–7]. Fe–Si silicides with various compositions have been synthesized and characterized, such as thermodynamically stable  $\text{Fe}_3\text{Si}$ , FeSi, and  $\beta\text{-FeSi}_2$  and metastable  $\text{Fe}_2\text{Si}$ ,  $\text{Fe}_5\text{Si}_3$ , and  $\alpha\text{-FeSi}_2$  [8–12]. According to the Fe–Si phase diagram [13],  $\text{Fe}_3\text{Si}$  exists in a wide stoichiometric range from 10 to 29.8 at.% Si but the homogeneity range of FeSi is very narrow. Both phases coexist between 25 and 50 at.% Si. The disilicide  $\text{FeSi}_2$  of  $\beta$  phase is a line compound at 66.7 at.% Si and is stable at room temperature, while  $\alpha$ -phase  $\text{FeSi}_2$  forms within 70–73.5 at.% Si at temperatures above 937 °C [13].

Among the various fabrication methods for preparing transition metal silicides in a monolithic or composite form, self-propagating high-temperature synthesis (SHS) has the characteristics of simplicity, low energy requirement, short processing time, and high-purity products [14–16]. Furthermore, the high temperature gradient combined with rapid cooling makes the SHS reaction possible to produce metastable phases and unique structures. Unlike silicide compounds associated with molybdenum [17] and the transition metals of groups IVb and Vb [18,19], iron silicides cannot be produced by direct combustion of Fe and Si powders in the SHS mode due to weak reaction exothermicity. Consequently, mechanical and chemical activation on combustion synthesis has been considered as an alternative to

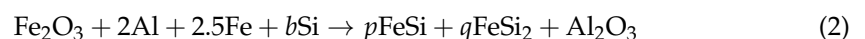
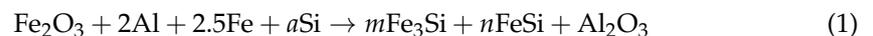
resolve this issue. For example, Gras et al. [20] employed mechanically activated Fe and Si powders, which were treated by high-energy ball milling, to produce FeSi and  $\beta$ -FeSi<sub>2</sub> through self-sustaining combustion synthesis. KNO<sub>3</sub> was adopted as a reaction promoter to chemically stimulate the combustion between Fe and Si powders on the synthesis of FeSi and  $\alpha$ -FeSi<sub>2</sub> [21]. On the other hand, mechanical alloying was utilized to fabricate FeSi- and Fe<sub>3</sub>Si-Al<sub>2</sub>O<sub>3</sub> composites from the SiO<sub>2</sub>/Al/Fe and Fe<sub>3</sub>O<sub>4</sub>/Al/Si powder mixtures, respectively [22,23]. The addition of a hard secondary phase, such as Al<sub>2</sub>O<sub>3</sub>, was shown to improve mechanical properties of iron silicides [22]. Moreover, Fe<sub>3</sub>Si-Al<sub>2</sub>O<sub>3</sub> composites exhibited good ferromagnetic behavior with hysteresis loops [23]. With the use of the SHS metallurgy method, FeSi-Al<sub>2</sub>O<sub>3</sub> composites with a molar ratio of FeSi/Al<sub>2</sub>O<sub>3</sub> ranging from 1.2 to 4.5 were recently produced from combining the reduction of Fe<sub>2</sub>O<sub>3</sub> and SiO<sub>2</sub> by Al with elemental Fe-Si reactions [24].

In addition to the SHS metallurgy, the sol-gel method and hot roll-bonding technique have been considered as the promising process for the fabrication of particles and composites. For example, Najafi et al. [25] synthesized zirconium carbide nanopowders by the sol-gel method in the alcoholic system, within which zirconium propoxide and phenolic resin were used as precursors of Zr and carbon, respectively. Functionally graded aluminum matrix Al6061/SiC<sub>p</sub> composite laminates were fabricated by successive hot roll-bonding, which utilized two composite layers as outer strips and a layer of Al1050 as interlayer [26].

This study aims to investigate the different phases of Fe-Si intermetallics formed within a wide stoichiometric range from Fe-20 to Fe-70.5 at.% Si by thermite-assisted combustion synthesis in the SHS mode. By taking advantage of the highly exothermic thermite reaction of Fe<sub>2</sub>O<sub>3</sub> with Al, the formation of in situ Fe-Si intermetallics/Al<sub>2</sub>O<sub>3</sub> composites was conducted with reactant powder compacts consisting of Fe<sub>2</sub>O<sub>3</sub>, Al, Fe, and Si. Effects of the Si percentage on the reaction exothermicity, combustion temperature, flame-front propagation velocity, and phase composition and microstructure of the iron silicides/Al<sub>2</sub>O<sub>3</sub> composites were explored. Moreover, the activation energy of the SHS reaction was determined from combustion wave kinetics.

## 2. Materials and Methods

The starting materials adopted by this study comprised Fe (Alfa Aesar Co., Ward Hill, MA, USA, <45  $\mu$ m, 99.5%), Si (Strem Chemicals, Newburyport, MA, USA, <45  $\mu$ m, 99.5%), Al (Showa Chemical, Tokyo, Japan, <45  $\mu$ m, 99.9%), and Fe<sub>2</sub>O<sub>3</sub> (Alfa Aesar Co., <45  $\mu$ m, 99.5%). Based on the atomic proportions between Fe and Si in the reactant mixtures, two combustion systems expressed as Reactions (1) and (2) were considered.



Reactant mixtures were composed of thermite reagents of Fe<sub>2</sub>O<sub>3</sub> + 2Al and metallic Fe and Si powders. Reaction (1) was formulated with the Si percentage from Fe-20% to Fe-45% Si, within which Fe<sub>3</sub>Si and FeSi was considered as silicide compounds to be produced. Reaction (2) was designed for Fe/Si stoichiometry from Fe-50% to Fe-70.5% Si and the resulting silicides of Reaction (2) could be FeSi and FeSi<sub>2</sub>.

With respect to different Si percentages denoted by  $x$  of Fe- $x$ % Si, Tables 1 and 2 list the values of stoichiometric coefficients, including  $a$ ,  $m$ , and  $n$ , of Reaction (1) and  $b$ ,  $p$ , and  $q$  of Reaction (2). These values were calculated based on the conservation of atomic species, except for two off-stoichiometric conditions. One is Reaction (1) of Fe-20% Si in Table 1, which represents an under-stoichiometric condition (i.e., a Si-lean composition) to produce Fe<sub>3</sub>Si because Fe<sub>3</sub>Si exists in a wide homogeneity range from 10 to 29.8 at.% Si. The other is Reaction (2) of Fe-70.5% Si in Table 2 for the production of FeSi<sub>2</sub>. This case was intended for FeSi<sub>2</sub> of the  $\alpha$  phase since  $\alpha$ -FeSi<sub>2</sub> is an over-stoichiometric (i.e., Si-rich) disilicide and is present within a region of 70–73.5 at.% Si.

**Table 1.** Stoichiometric coefficients ( $a$ ,  $m$ , and  $n$ ) and adiabatic temperatures ( $T_{ad}$ ) of Reactions (1) under different Si percentages ( $x$ ) in terms of Fe- $x\%$ Si.

$x$ , Fe- $x\%$ Si	$a$	$m$	$n$	$T_{ad}$ (K)
20	1.13	1.13	0	2870
25	1.5	1.5	0	3206
30	1.93	1.29	0.64	3158
35	2.42	1.04	1.38	3110
40	3.0	0.75	2.25	3059
45	3.68	0.41	3.27	3008

**Table 2.** Stoichiometric coefficients ( $b$ ,  $p$ , and  $q$ ) and adiabatic temperatures ( $T_{ad}$ ) of Reactions (2) under different Si percentages ( $x$ ) in terms of Fe- $x\%$ Si.

$x$ , Fe- $x\%$ Si	$b$	$p$	$q$	$T_{ad}$ (K)
50	4.5	4.5	0	2960
55	5.5	3.5	1.0	2820
60	6.75	2.25	2.25	2670
65	8.36	0.64	3.86	2504
66.7	9.0	0	4.5	2444
70.5	10.75	0	4.5	2292

The reaction exothermicity of Reactions (1) and (2) was studied by calculating their adiabatic combustion temperature ( $T_{ad}$ ) as a function of  $x$  in Fe- $x\%$  Si, based on the following energy balance equation [27] with thermochemical data taken from [28,29].

$$\Delta H_r + \int_{298}^{T_{ad}} \sum n_j c_p(P_j) dT + \sum_{298-T_{ad}} n_j L(P_j) = 0 \quad (3)$$

where  $\Delta H_r$  is the reaction enthalpy at 298 K,  $n_j$  is the stoichiometric coefficient,  $c_p$  and  $L$  are the heat capacity and latent heat, and  $P_j$  refers to the product.  $\Delta H_r$  was calculated from the heats of formation of the reactants and products. Heats of formation for  $Fe_2O_3$ ,  $Al_2O_3$ ,  $Fe_3Si$ ,  $FeSi$ , and  $FeSi_2$  are  $-823.4$ ,  $-1675.7$ ,  $-73.1$ ,  $-79.4$ , and  $-81.2$  kJ/mol, respectively. Specific heats,  $c_p$  (in J/mol·K), of the product species as a function of temperature are given below [28,29].

$$c_p(Al_2O_3) = 117.49 + 10.38 \cdot 10^{-3} \cdot T - 3.71 \cdot 10^6 \cdot T^{-2} \quad (4)$$

$$c_p(Fe_3Si) = 80.2 + 25.7 \cdot 10^{-3} \cdot T - 0.2 \cdot 10^6 \cdot T^{-2} \quad (5)$$

$$c_p(FeSi) = 44.6 + 14.72 \cdot 10^{-3} \cdot T - 0.11 \cdot 10^6 \cdot T^{-2} \quad (6)$$

$$c_p(FeSi_2) = 64.2 + 20.6 \cdot 10^{-3} \cdot T - 0.15 \cdot 10^6 \cdot T^{-2} \quad (7)$$

In this study, the reactant powders were dry mixed in a tumbler ball mill (Quancin Tech. Co., Tainan, Taiwan), which consisted of a cylinder partially filled with raw materials and alumina grinding balls rotating about its longitudinal axis. The diameter of the grinding ball was 2.5 mm. The tumbler mill machine operated at 60 rpm and the milling time was 4 h. The purpose of this ball milling process was to disperse the agglomerated particles and to achieve the good mixing of the reactant powders. The action of ball milling in this study did not affect the size and shape of the particles. Well-mixed powders were uniaxially compressed to form cylindrical test specimens with 7 mm in diameter, 8.5 mm in height, and a relative density of 55%.

The SHS experiment was conducted in a windowed combustion chamber filled with high-purity (99.99%) argon at 0.2 MPa. The ignition was accomplished by a heated tungsten coil with a voltage of 60 V and a current of 1.5 A. The propagation rate of combustion wave ( $V_f$ ) was measured by recording the whole combustion event with a color CCD camera at 30 frames per second. The exposure time of each recorded image was set at

0.1 ms. To facilitate the accurate measurement of instantaneous locations of the combustion front, a beam splitter (Rolyn Optics; Covina, CA, USA), with a mirror characteristic of 75% transmission and 25% reflection, was used to optically superimpose a scale onto the image of the test sample. The combustion temperature was measured by an R-type (Pt/Pt-13%Rh) fine-wire thermocouple (Omega Engineering Inc.; Norwalk, CT, USA) with a bead size of 125  $\mu\text{m}$ . The details of the experimental setup were reported elsewhere [30].

The phase constituents of the synthesized products were analyzed by an X-ray diffractometer (Bruker D2 Phaser; Billerica, MA, USA) with  $\text{CuK}\alpha$  radiation. Scanning electron microscopy (SEM) analysis was performed (Hitachi S3000H; Tokyo, Japan) with energy dispersive spectroscopy (EDS) to examine the microstructure and elemental composition on the fracture surface of the final product. The open porosity of the product was determined by the Archimedes method. Vickers hardness ( $H_v$ ) measurements were conducted with 1.0 kg load for selected samples.

The activation energy ( $E_a$ ) of the SHS reaction was deduced from the temperature dependence of combustion wave velocity. The combustion wave velocity derived from an energy equation with a heat source can be expressed as [31,32]

$$V_f^2 = \frac{2\lambda}{\rho Q} \frac{RT_c^2}{E_a} k_o \exp(-E_a/RT_c) \quad (8)$$

where  $\lambda$  is the thermal conductivity,  $\rho$  the density,  $R$  the gas constant,  $Q$  the heat of reaction,  $T_c$  the combustion front temperature, and  $k_o$  the Arrhenius rate constant. According to Equation (8),  $E_a$  can be obtained from the slope of a best-fitted linear line correlating  $\ln(V_f/T_c)^2$  with  $1/T_c$ .

### 3. Results and Discussion

#### 3.1. Combustion Exothermicity and Combustion Wave Kinetics

The calculated values of  $T_{ad}$  are presented in Table 1 and indicate that  $T_{ad}$  of Reaction (1) decreases with increasing Si percentage except for the off-stoichiometric case of Fe-20% Si. For Reaction (1), the decrease of  $T_{ad}$  was mainly attributed to the increase of the numbers of mole of iron silicides ( $m + n$ ) formed in the products. Since the formation of iron silicides is less exothermic than aluminothermic reduction of  $\text{Fe}_2\text{O}_3$ , the overall exothermicity of combustion synthesis tends to decrease as the amount of silicide compounds increases. The exception was due to a smaller amount of  $\text{Fe}_3\text{Si}$  ( $m = 1.13$ ) produced from the Si-lean sample of Fe-20% Si when compared to that ( $m = 1.5$ ) associated with the stoichiometric condition of Fe-25% Si.

On the other hand, the numbers of mole of iron silicides ( $p + q = 4.5$ ) synthesized from Reaction (2) are constant. As shown in Table 2, the increase of Si content leads to an increase in  $\text{FeSi}_2$  but a decrease in  $\text{FeSi}$ . Although both  $\text{FeSi}$  and  $\text{FeSi}_2$  have comparable enthalpies of formation, the heat capacity of  $\text{FeSi}_2$  is much larger than that of  $\text{FeSi}$ . This suggested lower formation exothermicity for  $\text{FeSi}_2$  and explained the decrease of  $T_{ad}$  with increasing Si percentage for Reaction (2).

Figure 1a,b illustrates two combustion sequences recorded from Reaction (1) of Fe-25% Si and Fe-40% Si, and Figure 1c,d is associated with Reaction (2) of Fe-50% Si and Fe-66.7% Si. It is evident that for all reactions a distinct combustion front formed upon ignition and propagated along the powder compact in a self-sustaining manner. A comparison unfolded that the sample of Figure 1a exhibits stronger combustion luminosity, the flame spreading time is shorter, and the final product is partially melted. The burned sample of Figure 1b essentially retained its original shape.

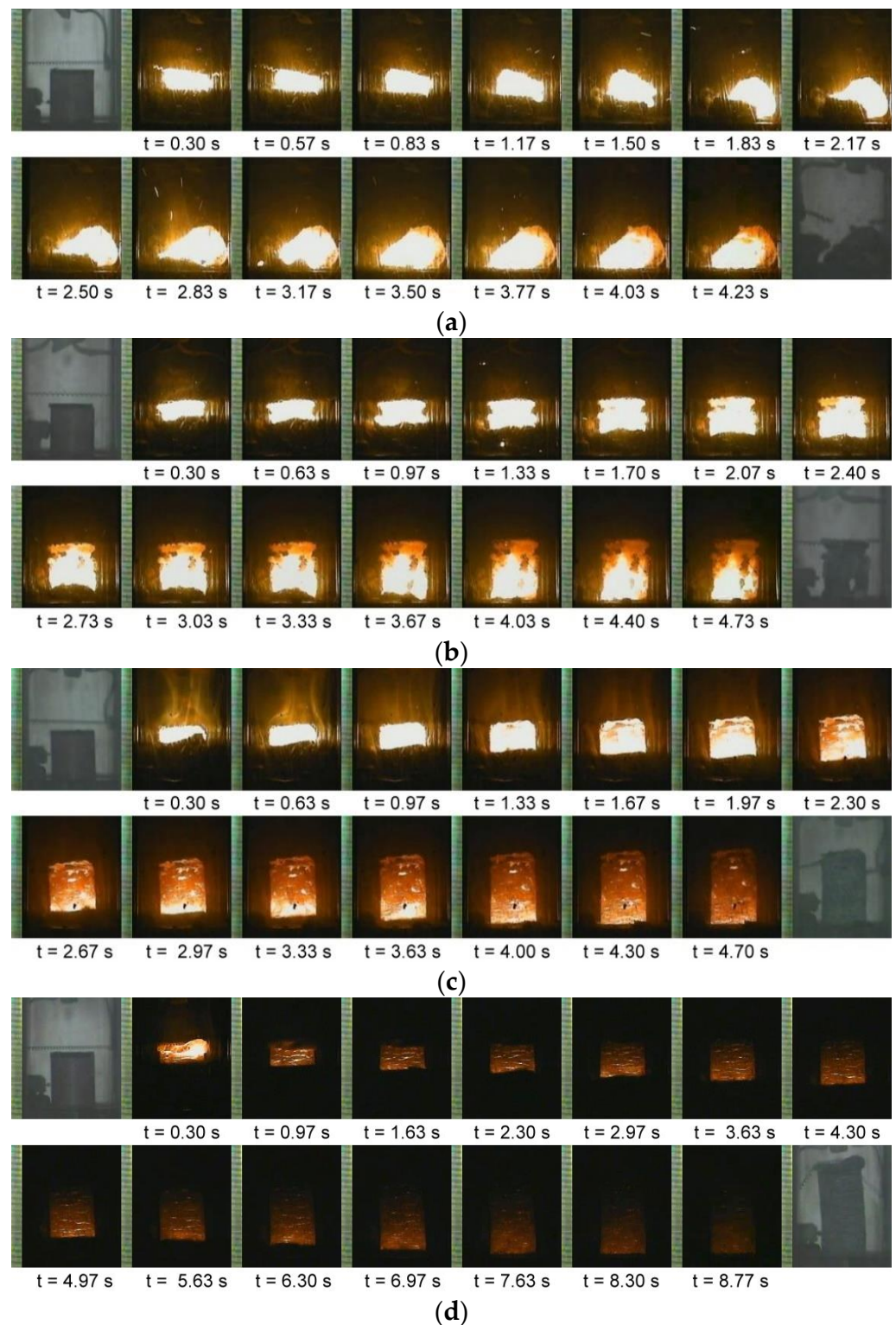
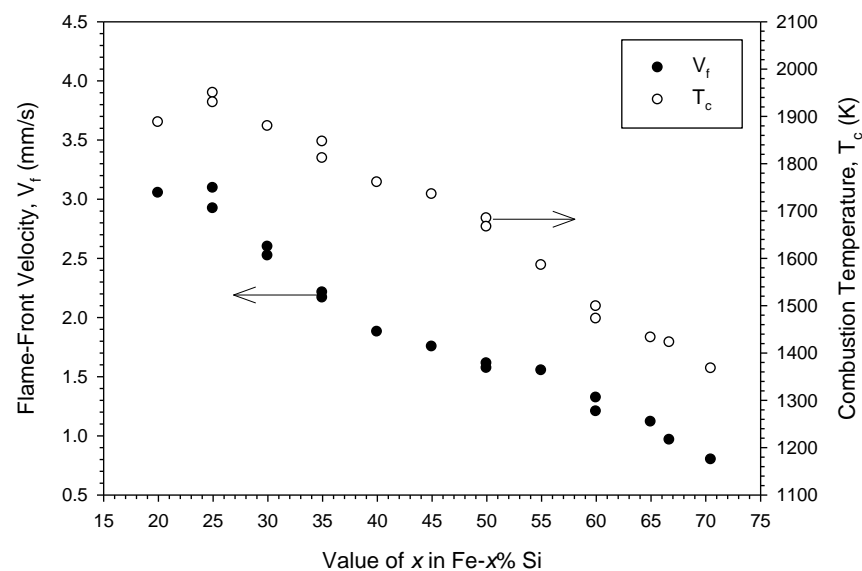


**Figure 1.** SHS combustion wave propagation sequences recorded from test samples of (a) Fe-25% Si, (b) Fe-40% Si, (c) Fe-50% Si, and (d) Fe-66.7% Si.

In Figure 1c,d, however, the combustion glow gradually fades away as the flame front progresses, the propagation time becomes longer, and the products are stretched out. These observations reflect vigorous combustion for Reaction (1) of Fe-25% Si. The partial melting of the burned sample of Reaction (1) with Fe-25% Si could be mainly attributable to the combustion temperature exceeding the melting point of  $\text{Fe}_3\text{Si}$  of about  $1210\text{ }^\circ\text{C}$  [13].

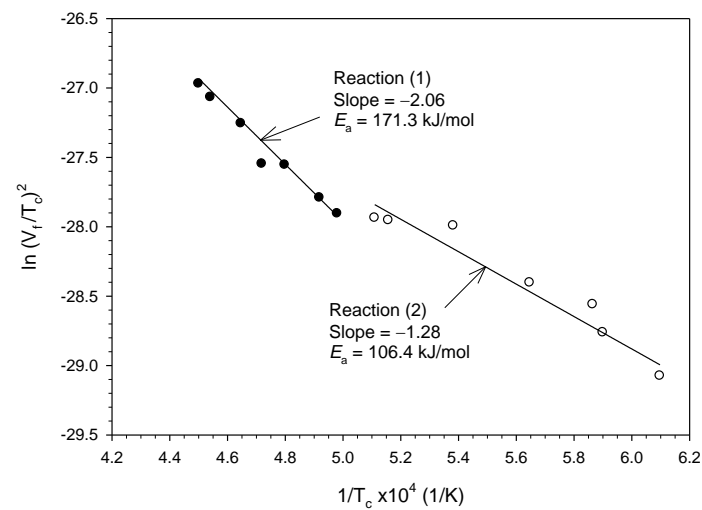
The elongated products obtained from Reaction (2) of Fe-50% Si and Fe-66.7% Si were due partly to the combustion temperature below the melting points of FeSi and FeSi<sub>2</sub> at 1410 and 1220 °C, respectively [13] and in part were interpreted as the combined result of the green compact porosity, small pores evolved from Kirkendall effect, and density change between the reactants and products [15].

The variations of flame-front propagation velocity ( $V_f$ ) and combustion front temperature ( $T_c$ ) with Si content of Fe- $x$ % Si for Reactions (1) and (2) are shown in Figure 2. As the Si proportion increased from Fe-25% to Fe-70.5% Si, it was noticed that  $V_f$  decreased from 3.1 to 0.8 mm/s and  $T_c$  declined from 1950 to 1367 K. The combustion wave propagation rate of the SHS process is mostly governed by the layer-by-layer heat transfer from the reaction zone to unburned region and therefore is subject to the combustion front temperature. This clarifies the consistency between combustion wave velocity and reaction front temperature. Moreover, the trend variation of  $T_c$  agrees reasonably with that of  $T_{ad}$ . In particular, Figure 2 indicates that  $T_c$  of Reaction (1) with Fe-20% Si of about 1890 K is lower than that of 1950 K reached by Reaction (1) with Fe-25% Si, confirming the lower reaction exothermicity of this under-stoichiometric sample.



**Figure 2.** Variations of flame-front velocity ( $V_f$ ) and combustion temperature ( $T_c$ ) with Si percentage of Fe- $x$ % Si of sample compacts.

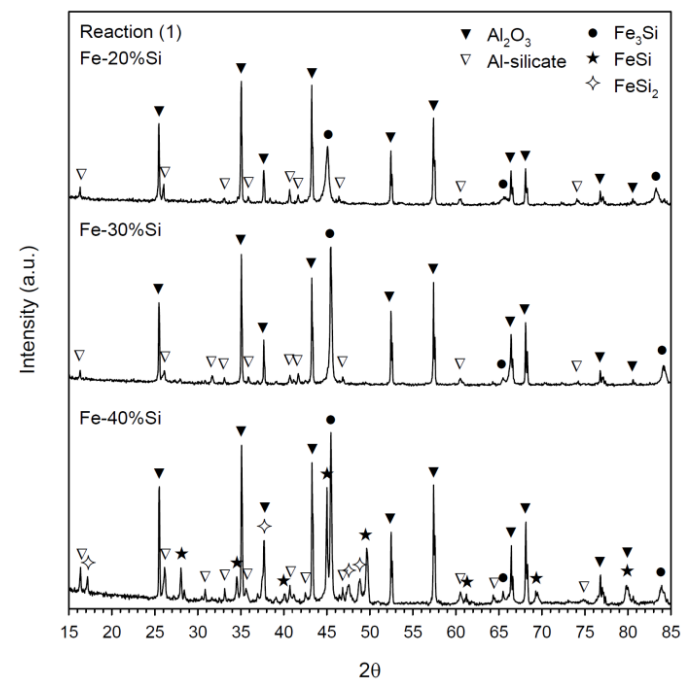
According to combustion wave kinetics, the activation energies ( $E_a$ ) of Reactions (1) and (2) were determined on the basis of the correlation between  $\ln(V_f/T_c)^2$  and  $1/T_c$ . Two sets of experimental data with their best-fitted linear lines are plotted in Figure 3. From the slopes of straight lines, the values of  $E_a$  equal to 171.3 and 106.4 kJ/mol were deduced for Reactions (1) and (2), respectively. The activation energy represents a kinetic barrier that depends on the reaction mechanism and transport phenomena. The possible reaction pathways of Reactions (1) and (2) were initiated by the aluminothermic reduction of Fe<sub>2</sub>O<sub>3</sub>. In addition to the kinetic aspect, the reduction of Fe<sub>2</sub>O<sub>3</sub> by Al was thermodynamically favorable and acted as the major heat-releasing step to sustain the SHS process. Different silicide phases formed from SHS reactions could be responsible for a larger  $E_a$  for Reaction (1) than Reaction (2).



**Figure 3.** Activation energies ( $E_a$ ) of Reactions (1) and (2) deduced from the correlation of combustion wave velocity ( $V_f$ ) with reaction temperature ( $T_c$ ).

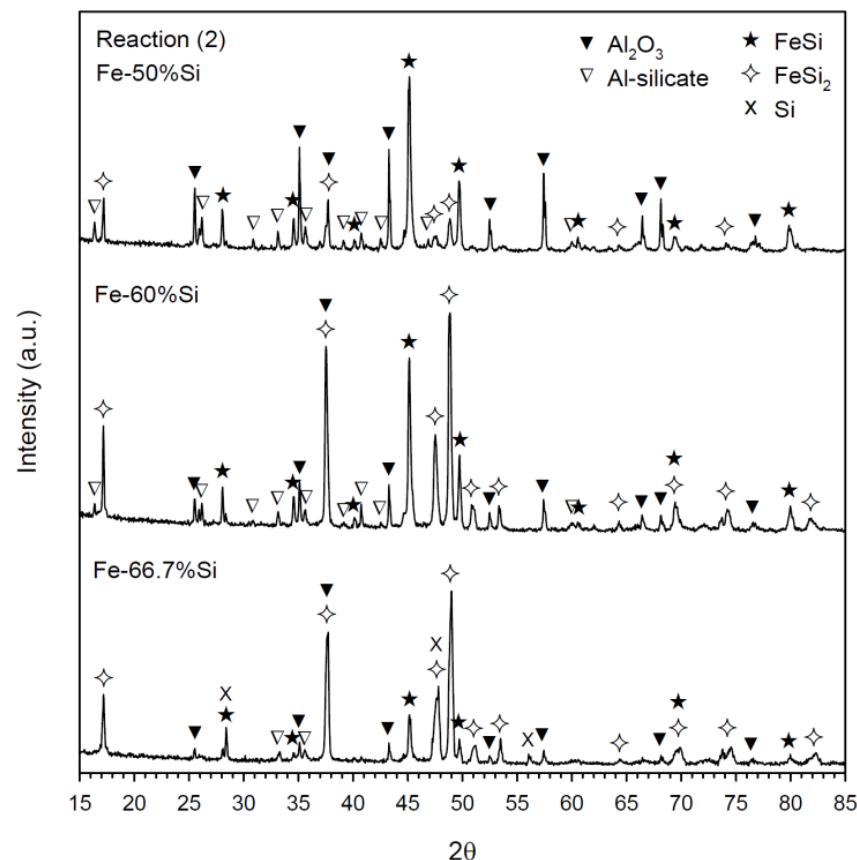
### 3.2. Phase Composition and Microstructure of Synthesized Products

Figure 4 presents XRD patterns of the products of Reaction (1) with Fe-20%, Fe-30%, and Fe-40% Si. As revealed in Figure 4,  $\text{Fe}_3\text{Si}$  is the only silicide formed from Reaction (1) with Fe-20% and Fe-30% Si. This agrees with the homogeneity range of  $\text{Fe}_3\text{Si}$  in the phase diagram. In the product of Reaction (1) with Fe-40% Si, silicide compounds comprising the three different phases of  $\text{Fe}_3\text{Si}$ ,  $\text{FeSi}$ , and  $\text{FeSi}_2$  were identified with  $\text{Fe}_3\text{Si}$  and  $\text{FeSi}$  being two primary phases. This reflects the fact that  $\text{Fe}_3\text{Si}$  and  $\text{FeSi}$  are co-existent under stoichiometry from Fe-30% to Fe-50% Si. In addition to silicide compounds, Figure 4 points out the formation of  $\text{Al}_2\text{O}_3$  from the aluminothermic reduction of  $\text{Fe}_2\text{O}_3$  and the presence of a small quantity of aluminum silicate that was formed through the dissolution of Si into  $\text{Al}_2\text{O}_3$  during the SHS process [33].



**Figure 4.** XRD patterns of SHS products of Reaction (1) with Si percentages of Fe-20% Si, Fe-30% Si, and Fe-40% Si.

Three XRD spectra depicted in Figure 5 show the phase compositions of the products of Reaction (2) with Fe-50%, Fe-60%, and Fe-66.7% Si. In addition to  $\text{Al}_2\text{O}_3$ , two silicide compounds, FeSi and FeSi<sub>2</sub>, were detected in Figure 5. FeSi was the major silicide and FeSi<sub>2</sub> the minor under stoichiometry of Fe-50% Si. It was evident that FeSi<sub>2</sub> substantially increased in the case of Fe-60% Si and became predominant over FeSi for a further increase in Si to Fe-66.7% Si. It should be noted that the FeSi<sub>2</sub> produced in this study is  $\alpha$ -phase disilicide. The formation of metastable  $\alpha$ -FeSi<sub>2</sub> was ascribed to the SHS process characterized by a unique temperature gradient starting with a sudden temperature rise over 1360 K and followed immediately by a rapid cooling process. Because of the presence of FeSi, a trivial amount of remnant Si was found in the final product of the reaction with Fe-66.7% Si.



**Figure 5.** XRD patterns of SHS products of Reaction (2) with Si percentages of Fe-50% Si, Fe-60% Si, and Fe-66.7% Si.

The yield percentage of different silicide phases ( $\text{Fe}_3\text{Si}$ , FeSi, and FeSi<sub>2</sub>) in the product was estimated by a semi-quantitative analysis based on the integrated intensity values of their highest XRD peaks, including  $\text{Fe}_3\text{Si}$  (220) at  $2\theta = 45.337^\circ$ , FeSi (210) at  $2\theta = 45.062^\circ$ , and FeSi<sub>2</sub> (102) at  $2\theta = 49.098^\circ$ . The yield percentage of silicide phases as a function of Si percentage is plotted in Figure 6. For Reaction (1),  $\text{Fe}_3\text{Si}$  was the only silicide produced from the samples with Si content from Fe-20% to Fe-30% Si. Iron silicides generated from the sample of Fe-35% Si contained 83%  $\text{Fe}_3\text{Si}$  and 17% FeSi. Three silicide compounds were present in the products of samples with Fe-40% and Fe-45% Si and the proportions of  $\text{Fe}_3\text{Si}/\text{FeSi}/\text{FeSi}_2$  were near to 60.0/45.3/4.7 and 26.7/67.3/6.0, respectively. It is evident for Reaction (1) that the dominant silicide shifted from  $\text{Fe}_3\text{Si}$  to FeSi as the Si percentage increased from Fe-20% to Fe-45% Si.

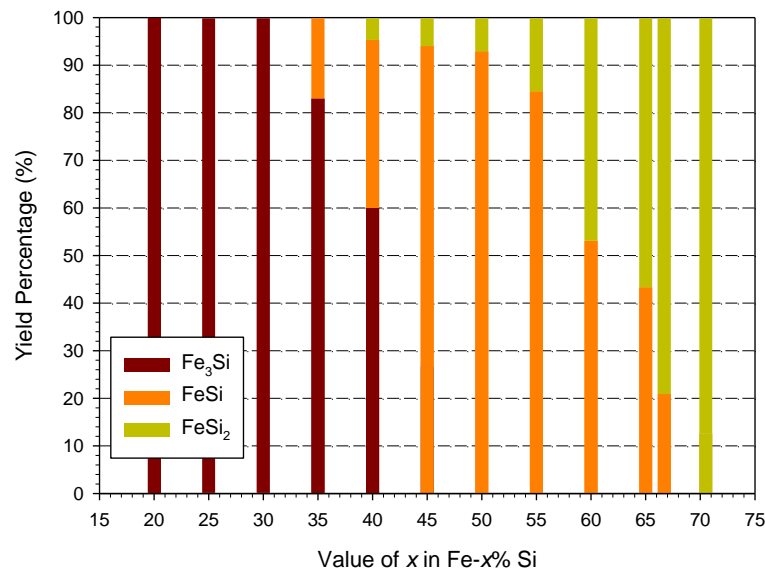


**Figure 6.** Yield percentages of iron silicides ( $\text{Fe}_3\text{Si}$ ,  $\text{FeSi}$ , and  $\text{FeSi}_2$ ) from samples with different Si percentages in  $\text{Fe-x}\%$  Si.

As also indicated in Figure 6, the resulting silicides of Reaction (2) with Fe-50% and Fe-55% Si were dominated by  $\text{FeSi}$  with a yield percentage up to 92.9% and 84.5%, respectively, and  $\text{FeSi}_2$  was the minor phase. With the increase of Si, comparable amounts of  $\text{FeSi}$  and  $\text{FeSi}_2$  were produced from the reactions of Fe-60% and Fe-65% Si. Finally,  $\text{FeSi}_2$  became the governing phase with high yield percentages of 79.1% and 87.4% in the products of samples with Fe-66.7% and Fe-70.5% Si, respectively. For Reaction (2) with Si from Fe-50% and Fe-70.5% Si, the change in dominant silicide from  $\text{FeSi}$  to  $\text{FeSi}_2$  was observed.

Figure 7a–c illustrates the SEM images and EDS spectra of the fracture surfaces of products synthesized from the samples with Si percentages of Fe-25% Si, Fe-50% Si, and Fe-70.5% Si, respectively. As can be seen in the SEM image of Figure 7a, the morphology exhibits granular particles distributing over a dense and continuous substrate and the particle size ranges approximately from 2 to 10  $\mu\text{m}$ . According to the EDS analysis, those particles were identified as iron silicide and the dense substrate was made up of aluminum oxide. The atomic ratio of Fe:Si based on the EDS spectrum of Figure 7a is 74.3:25.7, which is very close to 3:1 and proves the formation of  $\text{Fe}_3\text{Si}$  from the sample of Fe-25% Si. The dense matrix of Figure 7a is composed of Al and O elements with an atomic ratio of Al:O = 42.5:57.5, which matches reasonably with the stoichiometry of  $\text{Al}_2\text{O}_3$ .

Nearly spherical particles with a broad size range from submicron to about 10  $\mu\text{m}$  were observed in the SEM image of Figure 7b. The ratio of Fe:Si obtained from the EDS spectrum was about 47.7:52.3. This suggested the phase of  $\text{FeSi}$  and agreed reasonably with the starting Fe/Si stoichiometry of Fe-50% Si. The EDS spectrum associated with the dense substrate of Figure 7b indicates that constituent elements are Al and O. The composition of the matrix was confirmed to be  $\text{Al}_2\text{O}_3$  by the atomic ratio of Al:O = 37.9:62.1 deduced from the EDS analysis.

In Figure 7c, the SEM photo shows that many granular particles partially embedded in the dense substrate can be seen, most of them have a size of around 3  $\mu\text{m}$ , and some pores are formed in the  $\text{Al}_2\text{O}_3$  substrate. The EDS spectrum provided the atomic ratio of Fe:Si equal to 31.3:68.7, which is slightly Si-rich in comparison to the atomic composition of  $\text{FeSi}_2$ . This could be due to the fact that the silicide formed from the sample of Fe-70.5% Si is  $\alpha\text{-FeSi}_2$ , which is a Si-rich disilicide. Similarly, the EDS spectrum of Figure 7c shows that Al and O are two major constituent elements for the substrate and the atomic proportion of Al:O = 42.1:57.9 is in good agreement with that of  $\text{Al}_2\text{O}_3$ .

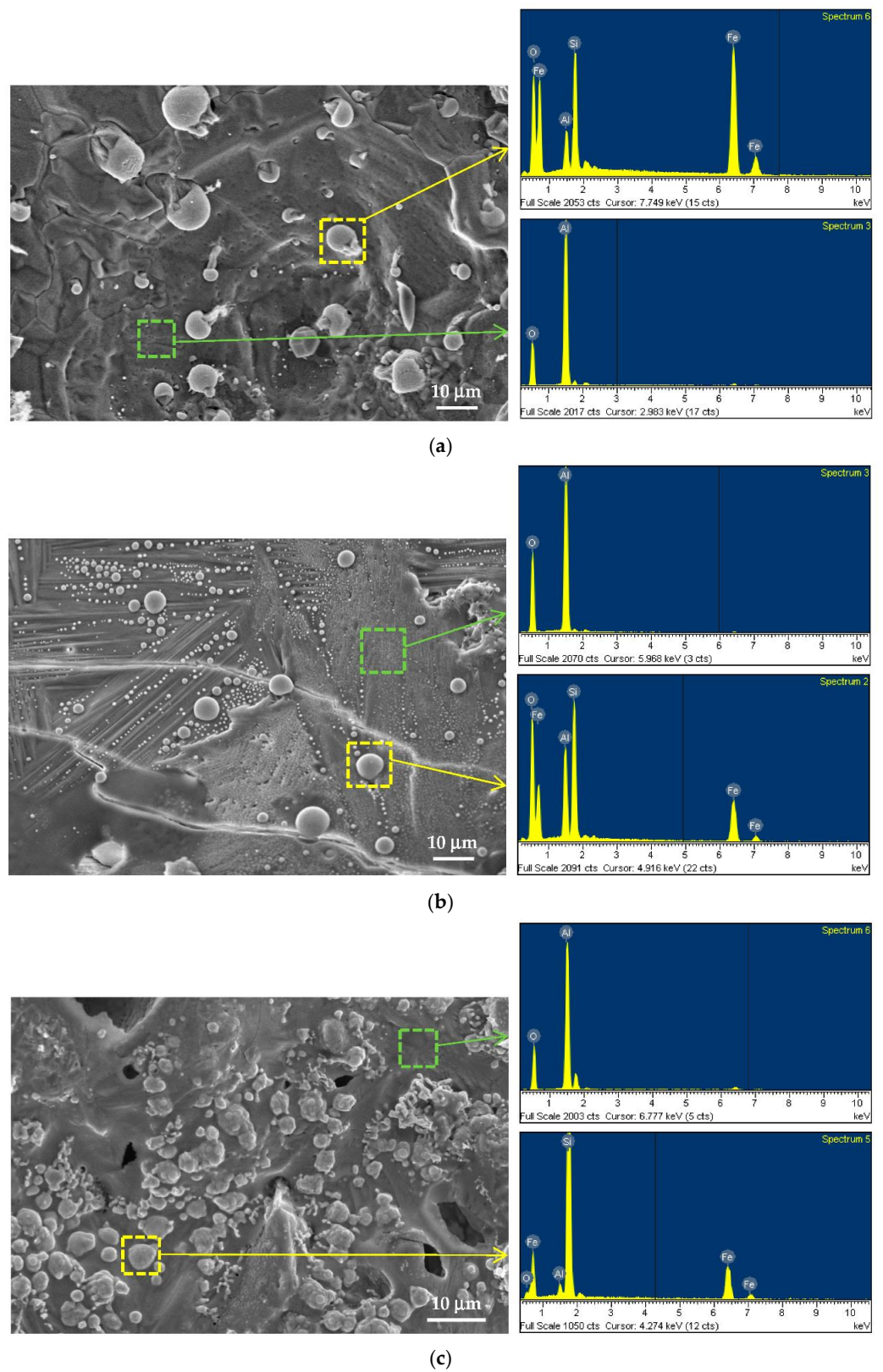


**Figure 7.** SEM micrographs and EDS spectra of SHS products of (a) Reaction (1) of Fe-25% Si, (b) Reaction (2) of Fe-50% Si, and (c) Reaction (2) of Fe-70.5% Si.

SEM images presented in Figure 8a–c are associated with the final composites produced from samples of Fe-20%, Fe-55%, and Fe-66.7% Si, respectively. It is evident that granular particles revealed in Figure 8a,b are more spherical than those in Figure 8c. The silicide grains formed were  $\text{Fe}_3\text{Si}$  in Figure 8a and mostly  $\text{FeSi}$  in Figure 8b. Their particle size ranged from submicron to about 10  $\mu\text{m}$ . The matrix made up of  $\text{Al}_2\text{O}_3$  in both Figure 8a,b is dense and continuous. Figure 8c shows that  $\text{FeSi}_2$  granules with a size of 2–5  $\mu\text{m}$  are formed over the  $\text{Al}_2\text{O}_3$  substrate. Some pores were observed in the matrix due to volume expansion of the product. A comparison between Figures 7 and 8 pointed out that similar microscopic structures of the final composites were observed as their initial compositions had close Fe/Si proportions.

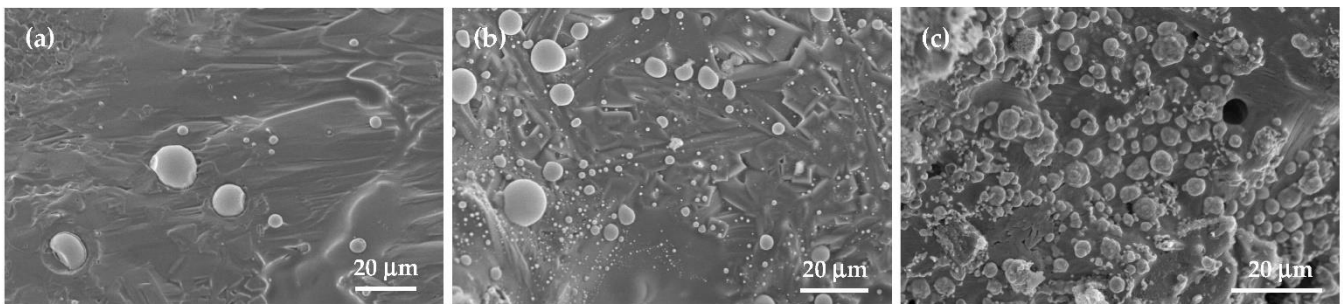


**Figure 8.** SEM micrographs of SHS products of (a) Reaction (1) of Fe-20% Si, (b) Reaction (2) of Fe-55% Si, and (c) Reaction (2) of Fe-66.7% Si.

For the reactions with Si percentage from Fe-20% to Fe-30% Si, their resulting  $\text{Fe}_3\text{Si}-\text{Al}_2\text{O}_3$  composites were produced in a partially melted form so that the porosity of  $\text{Fe}_3\text{Si}-\text{Al}_2\text{O}_3$  composites was relatively low and varied between 17% and 22%. Due to the slight volume expansion of the final products, the porosity of  $\text{FeSi}-\text{Al}_2\text{O}_3$  composites synthesized from samples of Fe-50% and Fe-55% Si was around 30%. Higher porosity of about 37–42% was attained for the  $\text{FeSi}_2-\text{Al}_2\text{O}_3$  composites produced from the reaction of Fe-66.7% and Fe-70.5% Si, because the products were prolonged after combustion. For selected composites obtained from the reactions with Fe-20%, Fe-50%, and Fe-66.7% Si, Vickers hardness measurements were conducted. The values of  $H_V$  were found to be 12.5, 10.4, and 7.6 GPa for the  $\text{Fe}_3\text{Si}$ -,  $\text{FeSi}$ -,  $\text{FeSi}_2-\text{Al}_2\text{O}_3$  composites, respectively.

#### 4. Conclusions

The formation of Fe–Si intermetallics– $\text{Al}_2\text{O}_3$  composites was investigated using thermite-assisted combustion synthesis with an emphasis on the relationship between iron silicide phases formed and initial Fe/Si proportions. Combustion reactions in the SHS mode were achieved with the powder compacts of the Fe/Si stoichiometry covering Si percentage from Fe-20% to Fe-70.5% Si. Results showed that the increase of Si content lowered the reaction exothermicity and decreased the combustion temperature from 1950 to 1367 K and flame-front propagation velocity from 3.1 to 0.8 mm/s. This was mainly due to the fact that the formation of iron silicide compounds was less exothermic than the aluminothermic reduction of  $\text{Fe}_2\text{O}_3$ . Depending on different iron silicides formed from the SHS reactions, two activation energies of 171.3 and 106.4 kJ/mol were determined. By means of XRD, three iron silicides,  $\text{Fe}_3\text{Si}$ ,  $\text{FeSi}$ , and  $\alpha\text{-FeSi}_2$ , were identified along with  $\text{Al}_2\text{O}_3$  in the final products.  $\text{Fe}_3\text{Si}$  was the only or major silicide for the reactions containing Si between Fe-20% and Fe-40% Si. Specifically,  $\text{Fe}_3\text{Si}$  was the only silicide in the products of Fe-20%, 25%, and 30% Si. The ratio of  $\text{Fe}_3\text{Si}/\text{FeSi}$  in the product generated from the sample of Fe-35% Si was 83/17. Three silicide compounds with a proportion of  $\text{Fe}_3\text{Si}/\text{FeSi}/\text{FeSi}_2$  was equal to 60.0/45.3/4.7, when produced from the sample of Fe-40% Si. The reactions of Fe-45%, Fe-50% and Fe-55% Si produced  $\text{FeSi}$  as the dominated silicide and the corresponding silicide compositions were  $\text{Fe}_3\text{Si}/\text{FeSi}/\text{FeSi}_2 = 26.7/67.3/6.0$ ,  $\text{FeSi}/\text{FeSi}_2 = 92.9/7.1$ , and  $\text{FeSi}/\text{FeSi}_2 = 84.5/15.5$ . For the reactions of Fe-65%, Fe-66.7%, and Fe-70.5% Si, their

resulting silicides comprised FeSi and  $\alpha$ -FeSi<sub>2</sub> and were predominated by  $\alpha$ -FeSi<sub>2</sub> which exhibited an increasing yield percentage from 56.7% to 79.1% and to 87.4%. The SEM images of the product fracture surface revealed that granular or nearly spherical silicides were distributed over or embedded partially in the dense substrate made up of Al<sub>2</sub>O<sub>3</sub>. The particle size of iron silicide grains varied from submicron to about 10  $\mu$ m and most of them were around 3–5  $\mu$ m. The phases of silicide grains, including Fe<sub>3</sub>Si, FeSi, and FeSi<sub>2</sub>, were also confirmed by the EDS analysis.

**Author Contributions:** Conceptualization, C.-L.Y.; methodology, C.-L.Y., A.L. and W.-C.L.; validation, C.-L.Y., A.L. and W.-C.L.; formal analysis, C.-L.Y., A.L. and W.-C.L.; investigation, C.-L.Y., A.L. and W.-C.L.; resources, C.-L.Y.; data curation, C.-L.Y., A.L. and W.-C.L.; writing—original draft preparation, C.-L.Y., A.L. and W.-C.L.; writing—review and editing, C.-L.Y.; supervision, C.-L.Y.; project administration, C.-L.Y.; funding acquisition, C.-L.Y. All authors have read and agreed to the published version of the manuscript.

**Funding:** This research work was funded by the Ministry of Science and Technology of Taiwan under the grant of MOST 110-2221-E-035-042-MY2.

**Institutional Review Board Statement:** Not applicable.

**Informed Consent Statement:** Not applicable.

**Data Availability Statement:** Data presented in this study are available in the article.

**Conflicts of Interest:** The authors declare no conflict of interest.

## References

1. Kauss, O.; Obert, S.; Bogomol, I.; Wablat, T.; Siemensmeyer, N.; Naumenko, K.; Krüger, M. Temperature resistance of Mo<sub>3</sub>Si: Phase stability, microhardness, and creep properties. *Metals* **2021**, *11*, 564. [[CrossRef](#)]
2. Vellios, N.; Keating, P.; Tsakiroopoulos, P. On the microstructure and properties of the Nb-23Ti-5Si-5Al-5Hf-5V-2Cr-2Sn (at.%) silicide-based alloy—RM(Nb)IC. *Metals* **2021**, *11*, 1868. [[CrossRef](#)]
3. Chumakova, L.S.; Bakulin, A.V.; Hocker, S.; Schmauder, S.; Kulkova, S.E. Interaction of oxygen with the stable Ti<sub>5</sub>Si<sub>3</sub> surface. *Metals* **2022**, *12*, 492. [[CrossRef](#)]
4. Wu, J.; Chong, X.Y.; Jiang, Y.H.; Feng, J. Stability, electronic structure, mechanical and thermodynamic properties of Fe-Si binary compounds. *J. Alloys Compd.* **2017**, *693*, 859–870. [[CrossRef](#)]
5. Sun, X.; Liu, X.; Liu, X.; Meng, Y.; Song, C.; Yang, Y.; Li, Y.W.; Wen, X.D. Exploration of properties from both the bulk and surface of iron silicides: A unified theoretical study. *J. Phys. Chem. C* **2019**, *123*, 11939–11949. [[CrossRef](#)]
6. Dahal, N.; Chikan, V. Phase-Controlled synthesis of iron silicide (Fe<sub>3</sub>Si and FeSi<sub>2</sub>) nanoparticles in solution. *Chem. Mater.* **2010**, *22*, 2892–2897. [[CrossRef](#)]
7. Wu, L.; Hu, F.; Yao, C.; Ding, B.; Xu, N.; Lu, M.; Sun, J.; Wu, J. Annealing effects and infrared photoelectric response of  $\beta$ -FeSi<sub>2</sub> on Si (100) substrate prepared by pulsed laser deposition. *Vacuum* **2021**, *188*, 110183. [[CrossRef](#)]
8. Comrie, C.M.; Falepin, A.; Richard, O.; Bender, H.; Vantomme, A. Metastable iron silicide phase formation by pulsed laser annealing. *J. Appl. Phys.* **2004**, *95*, 2365–2370. [[CrossRef](#)]
9. Meng, Q.S.; Fan, W.H.; Chen, R.X.; Munir, Z.A. Thermoelectric properties of nanostructured FeSi<sub>2</sub> prepared by field-activated and pressure-assisted reactive sintering. *J. Alloys Compd.* **2010**, *492*, 303–306. [[CrossRef](#)]
10. Qu, X.; Lü, S.; Hu, J.; Meng, Q. Microstructure and thermoelectric properties of  $\beta$ -FeSi<sub>2</sub> ceramics fabricated by hot-pressing and spark plasma sintering. *J. Alloys Compd.* **2011**, *509*, 10217–10221. [[CrossRef](#)]
11. Yeh, C.-L.; Chen, K.-T.; Shieh, T.-H. Effects of Fe/Si stoichiometry on formation of Fe<sub>3</sub>Si/FeSi-Al<sub>2</sub>O<sub>3</sub> composites by aluminothermic combustion synthesis. *Metals* **2021**, *11*, 1709. [[CrossRef](#)]
12. Guan, J.; Chen, X.; Yang, K.; Rykov, A.; Wang, J.; Liang, C. Preparation and size-dependent magnetism of highly dispersed iron silicide nanoparticles on silica. *J. Mater. Chem. C* **2014**, *2*, 5292–5298. [[CrossRef](#)]
13. Kubaschewski von Goldbeck, O. *Iron-Binary Phase Diagrams*; Springer: Berlin/Heidelberg, Germany, 1982; pp. 136–139.
14. Kamynina, O.; Vadchenko, S.; Shkodich, N.; Kovalev, I. Ta/Ti/Ni/Ceramic multilayered composites by combustion synthesis: Microstructure and mechanical properties. *Metals* **2022**, *12*, 38. [[CrossRef](#)]
15. Jiao, X.; Liu, Y.; Cai, X.; Wang, J.; Feng, P. Progress of porous Al-containing intermetallics fabricated by combustion synthesis reactions: A review. *J. Mater. Sci.* **2021**, *56*, 11605–11630. [[CrossRef](#)]
16. Vorotilo, S.; Potanin, A.Y.; Pogozhev, Y.S.; Levashov, E.A.; Kochetov, N.A.; Kovalev, D.Y. Self-propagating high-temperature synthesis of advanced ceramics MoSi<sub>2</sub>-HfB<sub>2</sub>-MoB. *Ceram. Int.* **2019**, *45*, 96–107. [[CrossRef](#)]
17. Minasyan, T.; Aghayan, M.; Liu, L.; Aydinyan, S.; Kollo, L.; Hussainova, I.; Rodríguez, M.A. Combustion synthesis of MoSi<sub>2</sub> based composite and selective laser sintering thereof. *J. Eur. Ceram. Soc.* **2018**, *38*, 3814–3821. [[CrossRef](#)]

18. Ran, H.; Niu, J.; Song, B.; Wang, X.; Feng, P.; Wang, J.; Ge, Y.; Farid, A. Microstructure and properties of  $Ti_5Si_3$ -based porous intermetallic compounds fabricated via combustion synthesis. *J. Alloys Compd.* **2014**, *612*, 337–342. [[CrossRef](#)]
19. Yeh, C.L.; Chen, W.H. An Experimental investigation on combustion synthesis of transition metal silicides  $V_5Si_3$ ,  $Nb_5Si_3$  and  $Ta_5Si_3$ . *J. Alloys Compd.* **2007**, *439*, 59–66. [[CrossRef](#)]
20. Gras, C.; Bernsten, N.; Bernard, F.; Gaffet, E. The mechanically activated combustion reaction in the Fe-Si system: In situ time-resolved synchrotron investigations. *Intermetallics* **2002**, *10*, 271–282. [[CrossRef](#)]
21. Gras, C.; Zink, N.; Bernard, F.; Gaffet, E. Assisted self-sustaining combustion reaction in the Fe-Si system: Mechanical and chemical activation. *Mater. Sci. Eng. A* **2007**, *456*, 270–277. [[CrossRef](#)]
22. Zakeri, M.; Rahimipour, M.R.; Sadrnezhad, S.K. In situ synthesis of  $FeSi-Al_2O_3$  nanocomposite powder by mechanical alloying. *J. Alloys Compd.* **2010**, *492*, 226–230. [[CrossRef](#)]
23. Guan, J.; Chen, X.; Zhang, L.; Wang, J.; Liang, C. Rapid preparation and magnetic properties of  $Fe_3Si-Al_2O_3$  nanocomposite by mechanical alloying and heat treatment. *Phys. Status Solidi A* **2016**, *213*, 1585–1591. [[CrossRef](#)]
24. Yeh, C.-L.; Chen, K.-T. Synthesis of  $FeSi-Al_2O_3$  composites by autowave combustion with metallothermic reduction. *Metals* **2021**, *11*, 258. [[CrossRef](#)]
25. Najafi, A.; Sharifi, F.; Mesgari-Abbasi, S.; Khalaj, G. Influence of pH and temperature parameters on the sol-gel synthesis process of meso porous  $ZrC$  nanopowder. *Ceram. Int.* **2022**, *48*, 26725–26731. [[CrossRef](#)]
26. Pouraliakbar, H.; Hosseini Monazzah, A.; Bagheri, R.; Seyed Reihani, S.M.; Khalaj, G.; Nazari, A.; Jandaghi, M.R. Toughness prediction in functionally graded  $Al6061/SiC_p$  composites produced by roll-bonding. *Ceram. Int.* **2014**, *40*, 8809–8825. [[CrossRef](#)]
27. Liang, Y.H.; Wang, H.Y.; Yang, Y.F.; Zhao, R.Y.; Jiang, Q.C. Effect of Cu content on the reaction behaviors of self-propagating high-temperature synthesis in  $Cu-Ti-B_4C$  system. *J. Alloys Compd.* **2008**, *462*, 238–248. [[CrossRef](#)]
28. Binnewies, M.; Milke, E. *Thermochemical Data of Elements and Compounds*; Wiley-VCH Verlag GmbH: Weinheim, Germany, 2002.
29. Acker, J.; Bohmhammel, K.; van den Berg, G.J.K.; van Miltenburg, J.C.; Kloc, C. Thermodynamic properties of iron silicides  $FeSi$  and  $\alpha-FeSi_2$ . *J. Chem. Thermodyn.* **1999**, *31*, 1523–1536. [[CrossRef](#)]
30. Yeh, C.L.; Lin, J.Z. Combustion synthesis of Cr-Al and Cr-Si intermetallics with  $Al_2O_3$  additions from  $Cr_2O_3-Al$  and  $Cr_2O_3-Al-Si$  reaction systems. *Intermetallics* **2013**, *33*, 126–133. [[CrossRef](#)]
31. Varma, A.; Rogachev, A.S.; Mukasyan, A.S.; Hwang, S. Combustion synthesis of advanced materials: Principals and applications. *Adv. Chem. Eng.* **1998**, *24*, 79–225.
32. Yeh, C.L.; Ke, C.Y. Combustion synthesis of  $FeAl-Al_2O_3$  composites with  $TiB_2$  and  $TiC$  additions via metallothermic reduction of  $Fe_2O_3$  and  $TiO_2$ . *Trans. Nonferrous Met. Soc. China* **2020**, *30*, 2510–2517. [[CrossRef](#)]
33. Radklaochotsatain, N.; Niyomwas, S.; Chanadee, T. Zirconium diboride-mullite composite form mineral: Combustion synthesis, consolidation, characterizations and properties. *Ceram. Int.* **2020**, *46*, 18842–18850. [[CrossRef](#)]